ADVANCED MATERIALS
www.advmat.de

Van der Waals Epitaxial Double Heterostructure: InAs/Single-Layer Graphene/InAs

Young Joon Hong, Jae Won Yang, Wi Hyoung Lee, Rodney S. Ruoff, Kwang S. Kim,* and Takashi Fukui*

Weak van der Waals (vdW) interactions have recently ignited diverse practical device applications, including heterojunction electronics,[1] mechanically transferrable optoelectronics,[2] and bio-molecular electronic devices.[3] Among the various materials for these applications, graphene offers an ideal material model for vdW attractions, because its carbon honeycomb monoatomic layer (with sp^2 hybridization) has no permanent polarity or surface dangling bonds (unpaired electrons). However, due to the chemical inertness of graphene,[4] fabrication of epitaxial semiconductor/graphene heterostructures has been difficult, with only very limited reactions for chemical binding, such as epitaxial oxidation.[5] Graphene-based vertical heterostructure devices, therefore, have been mostly fabricated by layer-by-layer stacking,[1] producing heterojunctions with random crystallographic orientations to the graphene lattices. This stacking technique has provided an important opportunity for high-performance graphene-based devices. Less layer–layer coupling at the heterojunction has only a slight effect on the sublattice symmetry; thus, this approach preserves the intrinsic properties of graphene and its high carrier mobility.[1,6] Due to the feasibility of large-scale synthesis of graphene[7] and monolithic integration of inorganic materials on graphene,[8] these promising heterostructure devices are now readily open to scale-up heteroepitaxial fabrication.

Koma et al. proposed that the vdW attractions can be exploited for heteroepitaxy on arbitrary substrates.[9] More importantly, vdW heteroepitaxy can be used to integrate a variety of inorganic materials on diverse substrates.[10] Recently, graphene was used as a substrate for semiconductor epitaxy by means of the vdW heteroepitaxy.[11] Specifically, because the vdW epitaxy yields an abrupt heterointerface with less electronic coupling, due to noncovalent bonding, it is surmised that the technique can provide a straightforward monolithic integration method for high-quality epitaxial semiconductor/graphene vertical heterostructures. For the graphene-based vertical multi-heterostructures, sequential direct vdW heteroepitaxy for each layer is necessary.[12] However, the high growth temperature required for the direct vdW epitaxy of graphene,[13] as well as the growth interruption for etching of the metal layer, limits the effectiveness and efficiency of microelectronic processing. Thus, there remains the challenge of developing new methods for fabricating the multi-heterostructures. To overcome these obstacles, we used suspended graphene substrates and the vapor-phase transport-based vdW epitaxy technique. In this communication, we demonstrate successful fabrication of epitaxial InAs/graphene/InAs double heterostructures, which is explained based on first-principle calculations.

Our promising approach to monolithically integrated graphene-based vertical double heterostructures is to grow InAs nanostructures on both sides of suspended single-layer graphene (S-SLG), using metal–organic vapor-phase epitaxy (MOVPE). For S-SLG substrate preparation, SLG films were synthesized by chemical vapor deposition (CVD)[14] and transferred onto the SiN_x membrane/Si substrates by etching–transfer techniques. The thickness of the S-SLG films was evaluated using micro-Raman spectroscopy (Supporting Information, Figure S1). The SiN_x membrane, with perforated hole arrays, was designed to support the S-SLG. Surface morphological inspection and microstructural analyses were performed by field-emission scanning electron microscopy (FESEM), high-resolution transmission electron microscopy (HRTEM), and atomic resolution scanning-TEM (STEM) with energy-dispersive X-ray spectroscopy (EDX). First-principles total energy, vdW binding energy, and electronic structure calculations were carried out using vdW-density functional (DF) method. Detailed descriptions of the experiments and theoretical calculations are given in Supporting Information.

The combined vdW–MOVPE yielded InAs nanostructures on both sides of S-SLG. **Figure 1**a illustrates the vapor-phase transport process for the vdW–MOVPE of InAs on/underneath the S-SLG. Low-pressure and high gas velocity transport conditions

Prof. Y. J. Hong
Department of Nanotechnology and Advanced Materials Engineering
Graphene Research Institute
and Hybrid Materials Research Center
Sejong University
Seoul, 143–747, Korea
E-mail: yjhong@sejong.ac.kr
Dr. J. W. Yang, Prof. K. S. Kim
Department of Chemistry
Center for Superfunctional Materials
Pohang University of Science and Technology (POSTECH)
Pohang, 790–784, Korea
E-mail: kim@postech.ac.kr
Prof. W. H. Lee
Department of Organic and Nano System Engineering
Konkuk University
Seoul, 143–701, Korea
Dr. W. H. Lee, Prof. R. S. Ruoff
Department of Mechanical Engineering and the Materials Science and Engineering Program
The University of Texas at Austin
Austin, TX, 78712, United States
Dr. Y. J. Hong, Prof. T. Fukui
Research Center for Integrated Quantum Electronics
Hokkaido University
Sapporo, 060–8628, Japan

DOI: 10.1002/adma.201302312

© 2013 WILEY-VCH Verlag GmbH & Co. KGaA, Weinheim

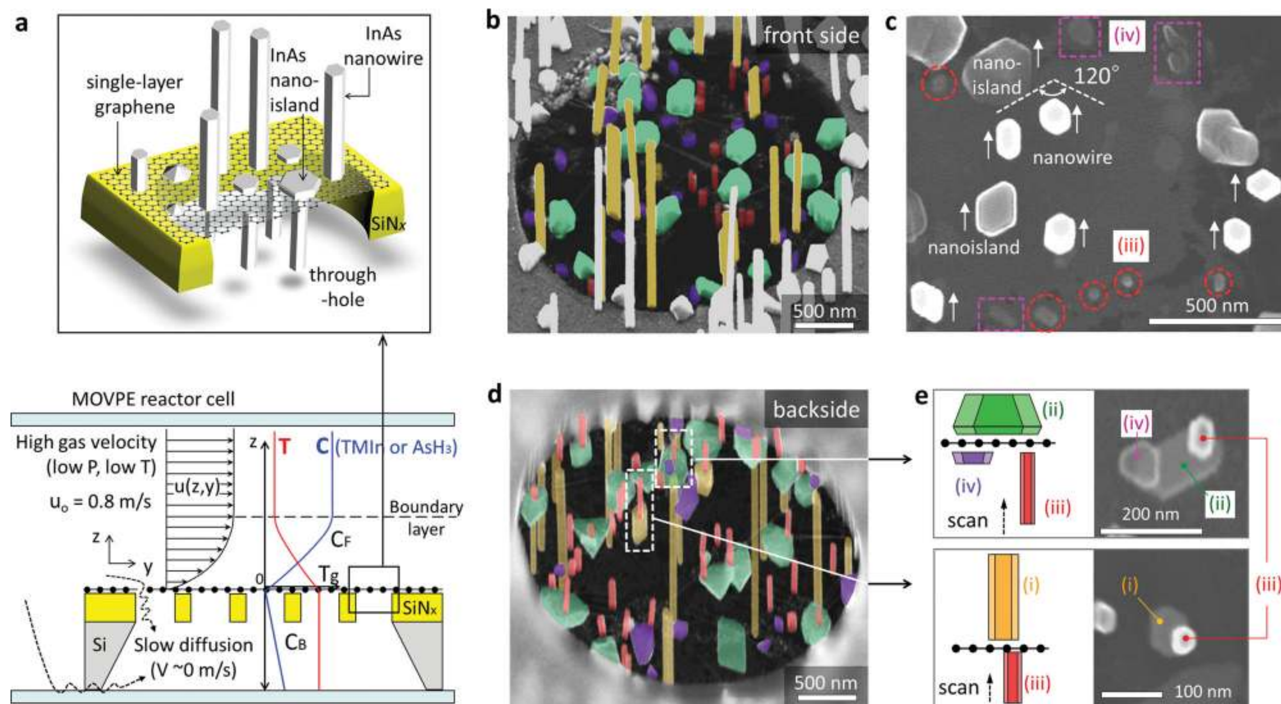

Figure 1. vdW–MOVPE growth of InAs nanostructures on/underneath S-SLG. (a) Schematic illustrations displaying InAs nanostructures grown on both sides of a S-SLG substrate by vdW–MOVPE. (b–e) FESEM images of the InAs nanostructures grown on S-SLG, taken from the front side (b, tilt-view; c, plan-view) and the backside (d, tilt-view; e, plan-views) of the membrane. The yellow (i) and green (ii) colors in (b–e) correspond to InAs nanowires and nanoislands formed on the front side of S-SLG, respectively; the red (iii) and violet (iv) colors are nanowires and nanoislands formed underneath the S-SLG, respectively. The red circles and violet boxes in (c) indicate nanowires and nanoislands formed on the backside of S-SLG, respectively, seen through the S-SLG. Dotted-line boxes in (d) highlight the InAs/s-SLG/InAs double heterostructures depicted in (e).

of 76 Torr and 0.8 m s^{-1}, respectively, were used to promote rapid diffusion of precursors across the thin boundary layer ($\delta \propto u_0^{-1/2}$ in the Blasius solution, where δ is the boundary layer thickness, and u_0 is the free-stream velocity).[15] The precursor afflux by diffusion enabled the growth of InAs on the backside of the S-SLG, with two possible diffusion-supply pathways: (i) through the gap between the substrate and the susceptor, and/or (ii) through the perforated holes in the membrane not covered with the S-SLG, as illustrated in Figure 1a.

The S-SLG was transparent enough to examine the InAs nanostructures formed on the backside of S-SLG under normal brightness and contrast conditions for SEM (Figure 1b–e, non-colored SEM images are also given in Figure S2). The FESEM images of Figure 1b and c show that vertically well-aligned InAs nanowires and nanoislands formed on both S-SLG and SLG/SiN_x, with a homogeneous six-fold rotational in-plane alignment, signifying that S-SLG, a free-standing ultrathin monoatomic layer, can provide sufficient vdW attractions for heteroepitaxy. Some of the nanoislands, however, had no hexagonal rotational symmetry, presumably due to multi-nucleations resulting in polycrystallinity at around grain boundary of the SLG. Because the nanostructures that formed underneath the S-SLG (red- and violet-colored objectives in Figure 1b) were smaller than those on the front side (Table S1), due to the low precursor concentration at the backside of S-SLG ($C_F > C_B$ in Figure 1a), further SEM inspection was performed on the backside of S-SLG. Figure 1d clearly shows high-density InAs nanostructures (≈5.5 × 10^8 cm^{-2}) formed on the backside of S-SLG, whose number density was comparable to that on the front side of the S-SLG (≈5.9 × 10^8 cm^{-2}). The number density values for the nanostructures are given in **Figure 2**. The number density values of respective nanostructures were the same within acceptable error ranges, irrespective of the substrate area, implying that the precursor concentration did not affect the heterogeneous nucleation density of InAs on either side of the S-SLG under vdW–MOVPE conditions but determined the mean size values of the nanostructures (Table S1). The same number density values resulted presumably from the same density of atomic ledges (or interplanar vacancies) on both the front and back of S-SLG.

The high-density formation of InAs nanostructures on both sides of S-SLG yielded InAs/SLG/InAs double heterostructures, in which the InAs crystals were diametrically grown at the same position on both sides of S-SLG (Figure 1d and e). The total number density of the double heterostructures was 3.2 × 10^8 cm^{-2}, which is half that of InAs nanostructures on S-SLG, indicating high yield (Figure 2a and c). The double heterostructures can be classified into nanowire/SLG/nanowire, nanoisland/SLG/nanowire, and nanoisland/SLG/nanoisland, in terms of morphology (Figure 1e). The nanostructures in these double heterostructures also exhibited an identical hexagonal in-plane alignment (SEM images in Figure 1e), attributable to the excellent lattice and symmetry match between InAs and graphene. Meanwhile, the InAs nanostructures on SLG/SiN_x exhibited little difference in number density, compared with those on S-SLG (Figure 2); this indicates that the amorphous

© 2013 WILEY-VCH Verlag GmbH & Co. KGaA, Weinheim
Adv. Mater. 2013,
DOI: 10.1002/adma.201302312

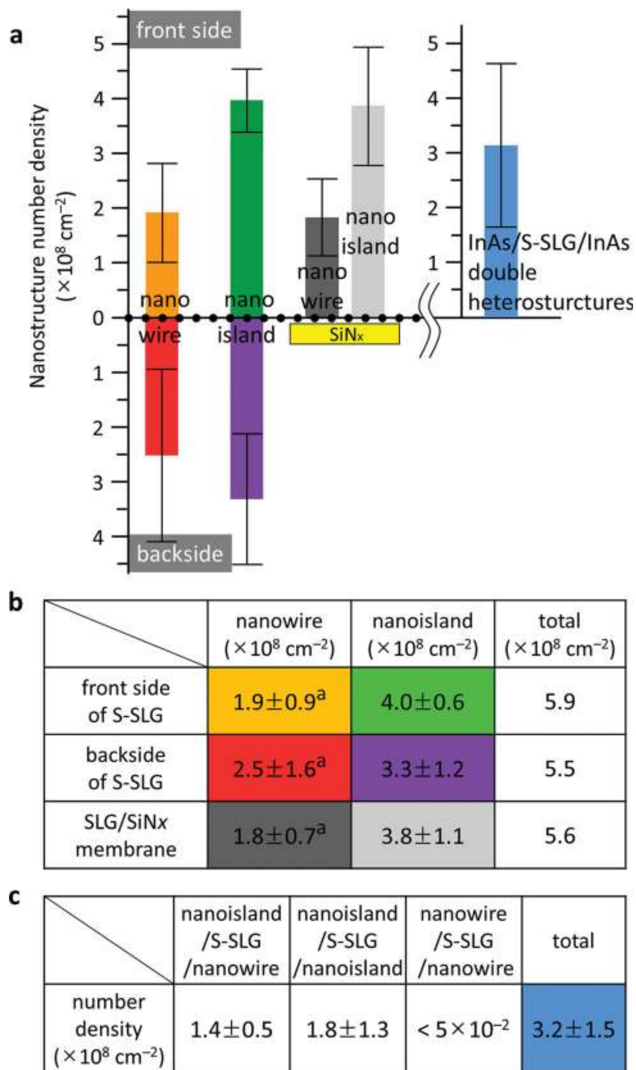

b

	nanowire ($\times 10^8$ cm^{-2})	nanoisland ($\times 10^8$ cm^{-2})	total ($\times 10^8$ cm^{-2})
front side of S-SLG	1.9±0.9[a]	4.0±0.6	5.9
backside of S-SLG	2.5±1.6[a]	3.3±1.2	5.5
SLG/SiNx membrane	1.8±0.7[a]	3.8±1.1	5.6

c

	nanoisland /S-SLG /nanowire	nanoisland /S-SLG /nanoisland	nanowire /S-SLG /nanowire	total
number density ($\times 10^8$ cm^{-2})	1.4±0.5	1.8±1.3	< 5×10^{-2}	3.2±1.5

Figure 2. Formation of InAs/S-SLG/InAs double heterostructures with high yield. (a) Histogram and (b) table displaying the number density of InAs nanostructures grown on S-SLG/SiN_x membrane substrates. The density values are classified by substrate area and morphology. (c) Table listing the number density of InAs/S-SLG/InAs double heterostructures. The values for nanowire in (b) are comparable to the nanowire number density of $(1.6 \pm 0.7) \times 10^8$ cm^{-2} reported in Ref. [11b] within an acceptable error range.

layers underneath the SLG provided little electrostatic attraction across the SLG films for forming InAs nanostructures, but the SLG significantly contributed to the epitaxy of InAs with sufficiently strong vdW force.

The crystallographic growth direction of InAs nanostructures grown by the vdW–MOVPE was investigated by cross-sectional high-angle annular dark-field (HAADF) STEM and EDX analyses. **Figure 3**a shows atomic resolution HAADF-STEM tomography and an EDX atomic-column mapping image recorded for an InAs nanowire, which reveal that the nanowire is composed of a zinc-blende/wurzite (ZB/WZ) mixture, similar to the microstructure of the nanowire grown by both conventional catalyst-free and metal-catalyst-assisted MOVPE.[16] Despite the high-density stacking faults in the nanowires, the As-polarized $[\bar{1}\bar{1}\bar{1}]_{ZB}$ or $[00\bar{1}]_{WZ}$ growth direction was maintained along the entire length. Analogously, single-crystalline InAs nanoislands exhibited the same trend of preferred crystallographic growth direction along $[\bar{1}\bar{1}\bar{1}]_{ZB}$ (Figure 3b). It is noted that the nanoislands are typically single-crystalline ZB in structure with a remarkably reduced density of stacking faults or polytypism, presumably due to the size-dependent thermodynamic stability of the compound semiconductors,[17] *e.g.*, III–V nanowires grown by covalent epitaxy[18] and II–VI nanoarchitectures grown via vdW epitaxy.[19] Cross-sectional STEM investigations revealed the formation of InAs nanostructures along the As-exposed direction, perpendicular to the surface of SLG; this suggests that the InAs/S-SLG/InAs double heterostructures exhibited polarity inversion at the vdW heterointerface, as schematically shown in Figure 3c.

It is necessary to determine how InAs nanostructures form exclusively along the As-terminated direction epitaxially on non-polar SLG. Plan-view TEM analyses of selected-area electron diffraction (SAED) patterns revealed a heteroepitaxial relationship of ZB-InAs $(\bar{1}\bar{1}\bar{1})[\bar{2}11]$||SLG (001)[100] (or WZ-InAs $(00\bar{1})[210]$||SLG (001)[100]) (Figure S3–S4). Considering the degree of semiconductor/graphene lattice misfit,[11d] InAs/SLG must satisfy one of three plausible binding sites for both In and As atoms on graphene: (i) on a hollow ('H'), which is the center of the carbon honeycomb, (ii) on top ('T'), directly above a carbon atom, or (iii) at the midpoint of the carbon–carbon bond bridge ('B') (Figure 3d). This suggests that the adsorption energy difference between In and As adatoms plays a crucial role in determining the crystallographic growth direction of InAs at the initial growth stage. According to atomic-resolution STEM analysis, the In atoms appeared to have been incorporated into the SLG surface, prior to the As atoms. Chan et al.[20] reported that In adatoms favorably occupy the 'H' sites for substantial energy savings, with higher coordination; this is in good agreement with our theoretical calculations. On the 'H' sites, the adsorption energy of In–SLG (–0.75 eV at equilibrium distance of 2.5 Å) was calculated to be much lower than that of As–SLG (–0.13 eV at equilibrium distance of 3.0 Å), suggesting that the initial bottom layer of In atoms, positioned close to the SLG, is energetically stable.

The vdW heterointerface was further explored using first-principles energy and electronic structure calculations. Based on the STEM analyses, we assumed that InAs nanostructures grow along ZB[111]B direction normal to the graphene surface. Not only for InAs(111)A free surface but also for the vdW epitaxial InAs(111)/SLG heterostructure, the total energy values of reconstructed interface (and surface) with In vacancy were calculated to be lower than those of unreconstruction, suggesting that the existence of an In vacancy in each (2 × 2) InAs (111)A interface is energetically preferable: the total energy of the (2 × 2)-InAs (111)A surface with In vacancy (= E^{v}_{InAs}) is lower than that of clean InAs (111)A (= E^{c}_{InAs}) by 1.151 eV; the total energy for the InAs(111)/SLG reconstructed with In vacancy (= $E^{v}_{interface}$) is lower than that of unreconstructed heterostructure (= $E^{c}_{interface}$) by 0.931 eV for the heterointerface (total energy values are given in **Table 1**). Using ab initio thermodynamic calculations,[21] the surface Gibbs free energy of the reconstructed InAs (111)/SLG heterointerface with In vacancies ($G^{v} = E^{v}_{interface} - (N_{In}-1)\mu_{In} - N_{As}\mu_{As} - N_{C}\mu_{C}$) was calculated to be lower than that of the non-reconstructed heterointerface

© 2013 WILEY-VCH Verlag GmbH & Co. KGaA, Weinheim

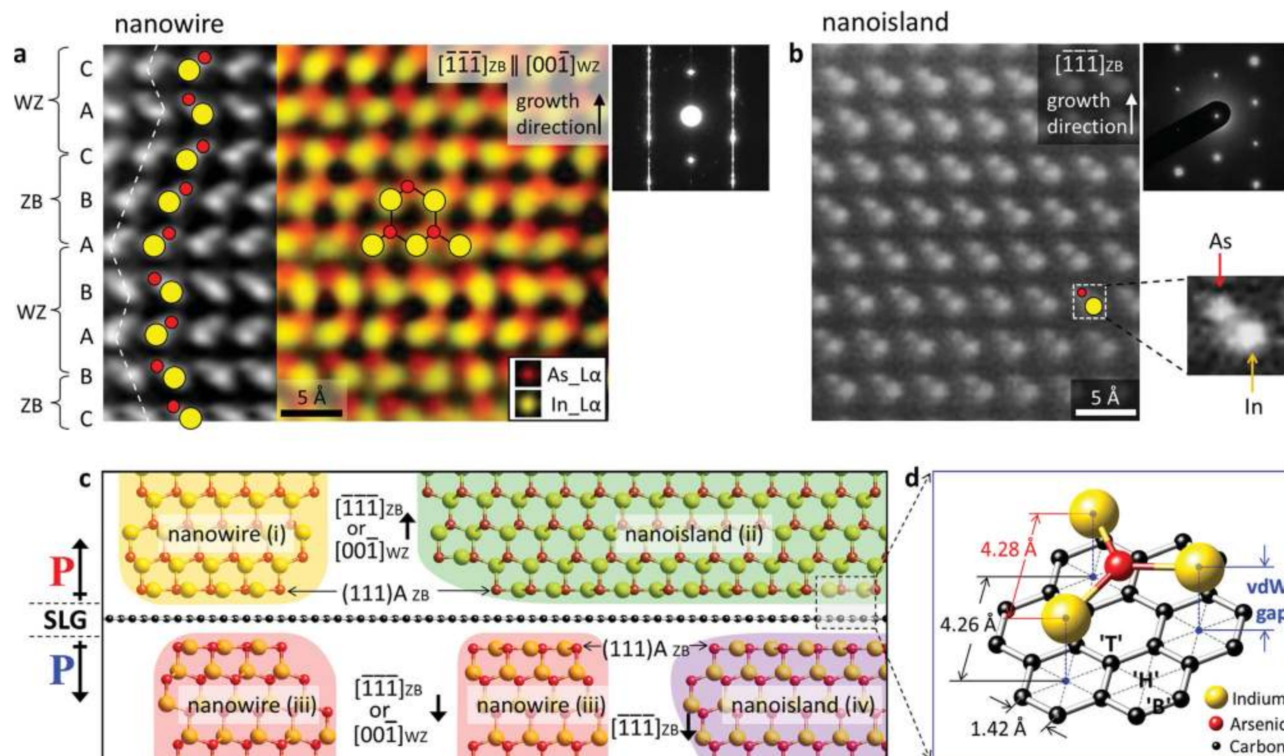

Figure 3. Preferred crystallographic growth direction of InAs on graphene substrates. (a) Cross-sectional atomic-resolution HAADF-STEM filtered image and EDX atomic-column mapping image of an InAs nanowire (yellow and red colors correspond to In and As, respectively). (b) HAADF-STEM image of InAs nanoislands. Insets of (a) and (b) are SAED patterns, showing that all of the images were taken along a $[1\bar{1}0]_{ZB}$-type projection. (c) Schematic atomic configurations depicting epitaxial InAs/SLG/InAs double heterostructures with polarity inversion. (d) Schematic atomic configuration of the vdW epitaxial InAs/graphene heterostructures. Three plausible configurations of In (or As) atoms on the hollow of a honeycomb, the top of a carbon atom, and the bond bridge of carbon–carbon are denoted as 'H', 'T', and 'B', respectively.

($G^c = E^c_{interface} - N_{In}\mu_{In} - N_{As}\mu_{As} - N_C\mu_C$), indicating that InAs(111) A interfaced to the SLG prefer to form the In vacancies for energy minimization (detailed descriptions of the calculations are given in Supporting Information). The theoretically-simulated vdW heterointerfacial atomic configurations are displayed in **Figure 4**a and b, presenting the vdW epitaxial InAs/SLG heterointerface with an In vacancy. The interfacial layer clearly shows that the As atoms near the In vacancy are intensely strained along the $-z$ direction for structural relaxation, so-called III–V vacancy buckling[22] verified by reflection high-energy electron diffraction and scanning tunneling electron microscopy for clean InAs (111)A surfaces under free surface vacuum conditions.[23] Because the flatly reconstructed InAs interfacial layer with an In vacancy has much less polarity along the z-direction than bulk InAs with a zigzag (111) In–As configuration, the reconstructed initial (111)A bottom layer is compatible with the non-polar graphene surface, in terms of its electron orbital hybridization. Importantly, because not only In atoms, but also As atoms, in the flatly reconstructed (111)A interface contributed to the stronger vdW attractions, the reconstructed binding energy (64 meV) was calculated to be ≈1.5 times as great as the non-reconstructed one (46 meV) (Table S2). A comparison of the total energy values for the heterointerface indicates the preference of the flatly reconstructed (111)A heterointerface formation. On top of the initial (111)A interfacial layer, InAs (111) layers are stacked along the [111]B direction with sp^3-bonds during the MOVPE process; this further confirms the formation of InAs nanostructures along the ZB [111]B direction normal to the graphene surface.

Table 1. Total energy values for vdW epitaxial InAs/SLG heterostructures.

	Clean InAs (111)A surface		InAs (111)/SLG heterointerfaces[b)]	
	Reconstruction with In vacancy in each (2×2) of InAs (111)A[a)]	No vacancy (no reconstruction)	Reconstruction with In vacancy in each (2×2) of InAs (111)A[a)]	No vacancy (no reconstruction)
Total energy	–41.726 (= E^v_{InAs})	–40.572(= E^c_{InAs})	–254.272 (= $E^v_{interface}$)	–253.341 (= $E^c_{interface}$)
vdW binding potential	–	–	–0.064 (= E_{vdW})	–

The energy values are given in eV unit. [a)]The reconstructed InAs (111)A surface (or interface) has almost flatten In–As configuration with an In vacancy in every (2 × 2) supercell; [b)]The bottommost layer of the heterostructure is InAs (111)A.

© 2013 WILEY-VCH Verlag GmbH & Co. KGaA, Weinheim
Adv. Mater. 2013,
DOI: 10.1002/adma.201302312

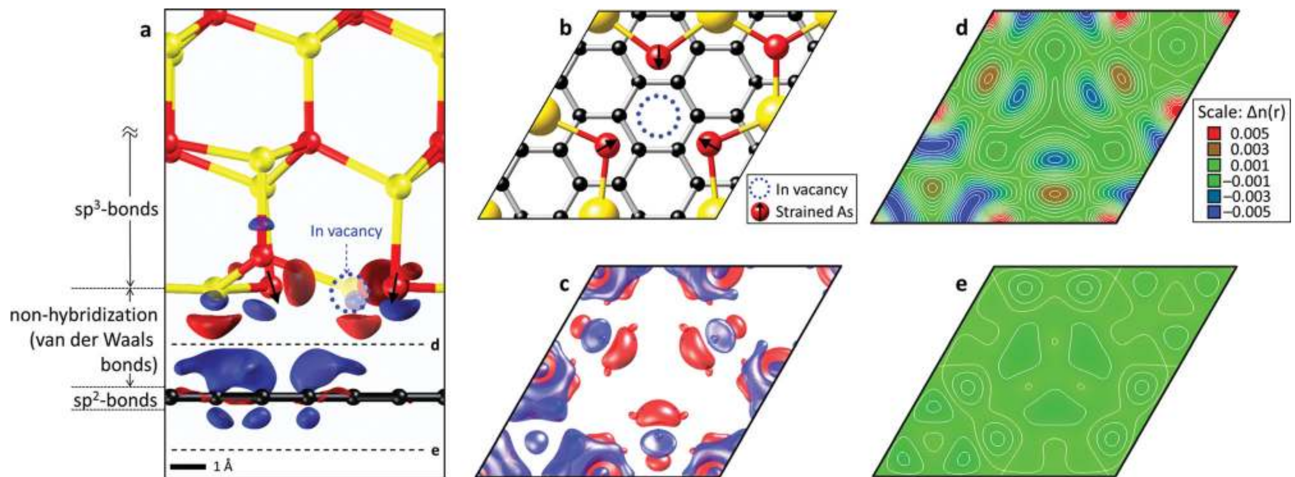

Figure 4. Electronic structure of the vdW epitaxial InAs/SLG heterointerface at equilibrium. (a) Molecular structures and CDD isosurfaces at the periphery of the vdW epitaxial InAs/SLG heterointerface. The red and blue CDD isosurfaces are contoured at the level of ±0.005e Å^{-3}, signifying electron accumulation and depletion, respectively. Plan-view of (b) atomic configuration of the epitaxial InAs(111)A/graphene heterointerface, (c) CDD isosurface map with an isovalue of ±0.005e Å^{-3}, and (d,e) contour maps of CDD calculated at a distance of ±1.55 Å from the SLG surface, as marked in (a). The diamond-shaped domain in (b–e) corresponds to the supercell of InAs(111)–(2×2) (or the graphene(001)–(2√3×2√3)) surface. Only the lowermost monolayer of InAs is shown in (b). Isolines in (d) and (e) are plotted at every 0.001e Å^{-3}. The electronic structure mapped by CDD represents the vdW binding feature with less electron orbital hybridization.

We also investigated the equilibrium vdW heterointerface gap and the vdW binding potential as a function of gap distance. The equilibrium vdW distance was examined by both HRTEM and vdW–DF calculations. **Figure 5**a shows a cross-sectional HRTEM image of the vdW heterointerface gap (≈0.31-nm separation), whose spacing is distinct from d_{002} of graphite (≈0.34 nm) and d_{111} (≈0.35 nm) of ZB InAs. Statistically, the equilibrium gap exhibited a narrow normal distribution, having a standard deviation of ±0.02 nm (Figure 5b). The energy diagram (Figure 5c) shows that the vdW binding energy has a maximum of 64 meV per carbon atom at the equilibrium heterointerface gap of 3.1 Å for the InAs/SLG heterostructure. The vdW gap of 3.1 ± 0.2 Å (Figure 5b) corresponds to a vdW binding energy of 61–64 meV in the potential diagram, implying homogeneous vdW binding over the entire heterointerface. Such a narrow, homogeneous vdW gap is attributed to maximized vdW cohesion, resulting from a flatly reconstructed InAs/SLG heterointerface with excellent commensuration. The vdW heteroepitaxial binding energy of InAs/SLG was calculated to be greater than the interplanar vdW binding energy of graphite (24–35 meV) obtained by experiments and theoretical calculations,[24] indicating that the quasi-vdW heteroepitaxial bonds are much stronger than the vdW homoepitaxial bonds. It is remarkable that the strong 'polar–nonpolar' quasi-vdW heteroepitaxy system of InAs/SLG broke the smallest limit of the interplanar vdW distance of graphene–graphene in graphite (3.4 Å).

Noticeably, despite the strong vdW heterointerface cohesion, no threading dislocations were observed at the abrupt heterointerface (Figure S5), presumably due to the sufficient stress relaxation through the noncovalent heterointerface. The vdW heteroepitaxy has great advantages for incommensurate heteroepitaxy with large lattice misfits because noncovalent heterointerfaces can effectually release the interfacial stress through the weakly-bound vdW heterojunctions. Hence, this noncovalent epitaxial feature enables to fabricate high quality epitaxial overlayers with suppressed threading dislocation density. Since the vdW heteroepitaxial systems with lattice misfits are under the incommensurate regime (homoepitaxial vdW structures are commensurate type), the InAs/graphene heterostructure is an incommensurate type. It is notable that no plural epitaxial relationships were observed in the plan-view TEM analysis since the InAs/graphene heterostructures have very small lattice misfit (≈0.47%). Therefore, we presume that the InAs/graphene is a nearly coherent (or nearly commensurate) vdW epitaxial type in the incommensurate regime. Importantly, not only the nearly commesurate vdW epitaxy in this study but also the incommensurate vdW epitaxy[25] yielded clean and abrupt heterointerfaces and high quality monocrystalline overlayers with no threading dislocations, all of which are a significant feature of vdW heteroepitaxy.[9b]

We further investigated the vdW binding energy for the epitaxial InAs/SLG/InAs double heterostructures. As presented in Figure 5c, the vdW binding potential of the double heterostructure was almost the same as that for the single heterostructure: the binding energy of InAs/SLG–InAs was calculated to be 66 meV per carbon atom at the equilibrium heterointerface gap of 3.1 Å for the double heterostructure. This implies that the backside of the SLG, facing away from the InAs nanostructure of the opposite side by 6.2 Å, is hardly affected by the InAs of front side, due to quite weak vdW attraction at the distance. Because there is little charge transfer from/into the front side of InAs at the vdW heterointerface (Figure 4c and d), charge density difference (CDD) maps of the SLG backside, shown in Figure 4e, are almost the same as that of a pristine SLG surface. Hence, the electronically decoupled backside of InAs/S-SLG can promote the formation of [111]B-oriented InAs, resulting in thermodynamically stable InAs/SLG/InAs double heterostructures with polarity inversion. This elucidates why double heterostructures are densely obtained on both sides of S-SLG.

As mentioned above, the vdW attraction enables the polarity inversion from the vdW heterojunction in the InAs/SLG/InAs

© 2013 WILEY-VCH Verlag GmbH & Co. KGaA, Weinheim

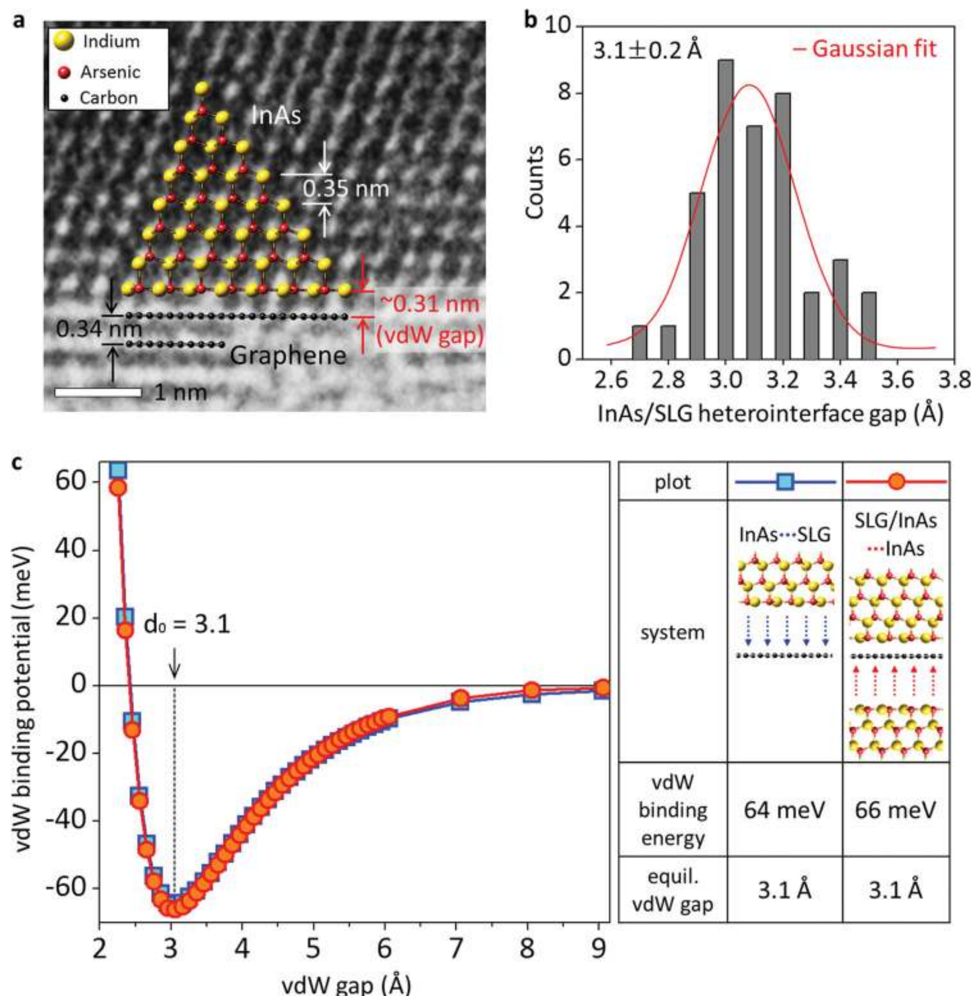

Figure 5. vdW gap of InAs/SLG heterostructures. (a) Cross-sectional HRTEM lattice image showing the InAs/graphene heterointerface gap. (b) Histogram of the InAs/SLG heterointerface gap, measured by HRTEM analyses. (c) vdW binding energy curves plotted as a function of the vdW gap for epitaxial InAs/SLG heterostructure and InAs/SLG/InAs double heterostructure, calculated by the vdW–DF method.

double heterostructures. It is well known that polarity inversion is expected when inserting a few nm-thick epitaxial metal or non-polar material layers during the growth of ZB or WZ crystal; this thick layer screens the electric field from the electric dipoles, whose heterointerfacial atoms are all connected by sp^3 bonds.[26] In contrast, in our quasi-vdW epitaxial system, the sp^2 hybrid orbital of SLG does not interact with the sp^3 bonds of InAs at the heterojunction in terms of chemical binding. Thus, even such an ultrathin conductive graphene layer (≈0.35-nm thickness) facilitates the polarity inversion for $sp^3/sp^2/sp^3$-type double heterostructures. Due to the decoupled chemical binding of the vdW epitaxy, the monoatomic layered substrates were not accompanied by antiphase heteroepitaxial structures, frequently observed in GaAs/Ge/GaAs double heterostructures with nonoctet-binding heterointerfaces.[27] This clarifies why single-domain (or single-crystalline) InAs nanostructures are easily obtained at the vdW heterojunctions, regardless of the graphene thickness (Figure S5).

In summary, a new approach for fabricating vdW epitaxial semiconductor/graphene double heterostructures was demonstrated using chemical vapor-phase transport-based vdW epitaxy of semiconductors on both sides of suspended graphene substrates. Electron microscopy investigations exhibited that the epitaxial formation of high-density InAs nanostructures on/underneath S-SLG resulted in the formation of InAs/SLG/InAs double heterostructures. Theoretical results from our first-principles calculations revealed that even though the double heterostructures possessed opposite polarizations (upward and downward), the vdW attraction was sufficiently strong and energetically favorable for epitaxial InAs/S-SLG/InAs double heterostructure formation. Additionally, a charge-screening effect was produced by conductive graphene due to noncovalent epitaxy. This quasi-vdW epitaxial system readily offers opportunities for the doping effect[28] investigations for functional device applications.[29] For fabricating exclusively the epitaxial nanowire/SLG/nanowire with desired spatial arrangements, the unwanted nanoisland formations should be suppressed by exploiting the selective-area vdW heteroepitaxy.[10b] We believe that this straightforward monolithic integration method for aligned crystallographic stacking will provide a new pathway for unconventional devices.

© 2013 WILEY-VCH Verlag GmbH & Co. KGaA, Weinheim
Adv. Mater. 2013, DOI: 10.1002/adma.201302312

Supporting Information

Detailed descriptions for the experiments and theoretical calculations are given. Raman spectra of S-SLG substrates (S1), non-colored FESEM images (S2), plan-view TEM (S3), simulated SAED analyses (S4), and cross-sectional HRTEM images of InAs/SLG (S5) are given in Supporting Figures. Supporting tables for morphological information of InAs nanowires/S-SLG (S1) and total energy values for the vdW epitaxial InAs/SLG heterostructures (S2) are also included. Supporting Information is available from the Wiley Online Library or from the author.

Acknowledgements

This work was financially supported by Priority Research Centers Program (2010–0020207) through the National Research Foundation of Korea (NRF) funded by the Ministry of Education, Science and Technology. Y.J.H and T.F acknowledge support from Japan Society for the Promotion of Science (JSPS) through the JSPS postdoctoral fellowship for foreign researchers (ID No. P11363). The research in POSTECH was supported by NRF (National Honor Scientist Program: 2010–0020414, WCU: R32–2008–000–10180–0) and KISTI (KSC-2011-G3–02). The authors thank Dr. Tomioka and Dr. Maebashi for their valuable support and discussion on MOVPE and TEM experiments.

Received: May 21, 2013
Revised: June 30, 2013
Published online:

[1] a) H. Wang, T. Taychatanapat, A. Hsu, K. Watanabe, T. Taniguchi, P. Jarillo-Herrero, T. Palacios, *IEEE Electron Device Lett.* **2011**, *32*, 1209–1211; b) L. Britnell, R. V. Gorbachev, R. Jalil, B. D. Belle, F. Schedin, A. Mishchenko, T. Georgiou, M. I. Katsnelson, L. Eaves, S. V. Morozov, N. M. R. Peres, J. Leist, A. K. Geim, K. S. Novoselov, L. A. Ponomarenko, *Science* **2012**, *335*, 947–950; c) W. J. Yu, Z. Li, H. Zhou, Y. Chen, Y. Wang, Y. Huang, X. Duan, *Nat. Mater.* **2012**, *12*, 246–252; d) H. Yang, J. Heo, S. Park, H. J. Song, D. H. Seo, K.-E. Byun, P. Kim, I. Yoo, H.-J. Chung, K. Kim, *Science* **2012**, *336*, 1140–1143.

[2] K. Chung, C.-H. Lee, G.-C. Yi, *Science* **2010**, *330*, 655–657.

[3] a) S. K. Min, W. Y. Kim, Y. Cho, K. S. Kim, *Nat. Nanotechnol.* **2011**, *6*, 162–165; b) N. Nerngchamnong, L. Yuan, D.-C. Qi, J. Li, D. Thompson, C. A. Nijhuis, *Nat. Nanotechnol.* **2013**, *8*, 113–118.

[4] Y. J. Shin, Y. Wang, H. Huang, G. Kalon, A. T. S. Wee, Z. Shen, C. S. Bhatia, H. Yang, *Langmuir* **2010**, *26*, 3798–3802.

[5] a) Y.-J. Kim, J. H. Lee, G.-C. Yi, *Appl. Phys. Lett.* **2009**, *95*, 213101; b) W. M. Choi, K.-S. Shin, H. S. Lee, D. Choi, K. Kim, H.-J. Shin, S.-M. Yoon, J.-Y. Choi, S.-W. Kim, *Nano Res.* **2011**, *4*, 440–447.

[6] C. R. Dean, A. F. Young, I. Meric, C. Lee, L. Wang, S. Sorgenfrei, K. Watanabe, T. Taniguchi, P. Kim, K. L. Shepard, J. Hone, *Nat. Nanotechnol.* **2010**, *5*, 722–726.

[7] S. Bae, H. Kim, Y. Lee, X. Xu, J.-S. Park, Y. Zheng, J. Balakrishnan, T. Lei, H. R. Kim, Y. I. Song, Y.-J. Kim, K. S. Kim, B. Özyilmaz, J.-H. Ahn, B. H. Hong, S. Iijima, *Nat. Nanotechnol.* **2010**, *5*, 574–578.

[8] a) H. Yoon, K. Seo, N. Bagkar, J. In, J. Park, J. Kim, B. Kim, *Adv. Mater.* **2009**, *21*, 4979–4982; b) D. H. Lee, J. E. Kim, T. H. Han, J. W. Hwang, S. Jeon, S.-Y. Choi, S. H. Hong, W. J. Lee, R. S. Ruoff, S. O. Kim, *Adv. Mater.* **2010**, *22*, 1247–1252; c) C.-H. Lee, Y.-J. Kim, Y. J. Hong, S.-R. Jeon, S. Bae, B. H. Hong, G.-C. Yi, *Adv. Mater.* **2011**, *23*, 4614–4619.

[9] a) A. Koma, K. Sunouchi, T. Miyajima, *Microelectron. Eng.* **1984**, *2*, 129–136; b) A. Koma, *Thin Solid Films* **1992**, *216*, 72–76.

[10] a) M. I. B. Utama, Z. Peng, R. Chen, B. Peng, X. Xu, Y. Dong, L. M. Wong, S. Wang, H. Sun, Q. Xiong, *Nano Lett.* **2011**, *11*, 3051–3057; b) Y. J. Hong, T. Fukui, *ACS Nano* **2011**, *5*, 7576–7584; c) M. I. B. Utama, Q. Zhang, S. Jia, D. Li, J. Wang, Q. Xiong, *ACS Nano* **2012**, *6*, 2281–2288; d) H. Peng, W. Dang, J. Cao, Y. Chen, D. Wu, W. Zheng, H. Li, Z.-X. Shen, Z. Liu, *Nat. Chem.* **2012**, *4*, 281–286; e) J. Pan, M. I. B. Utama, Q. Zhang, X. Liu, B. Peng, L. M. Wong, T. C. Sum, S. Wang, Q. Xiong, *Adv. Mater.* **2012**, *24*, 4151–4156.

[11] a) W. Dang, H. Peng, H. Li, P. Wang, Z. Liu, *Nano Lett.* **2010**, *10*, 2870–2876; b) Y. J. Hong, W. H. Lee, Y. Wu, R. S. Ruoff, T. Fukui, *Nano Lett.* **2012**, *12*, 1431–1436; c) Y. Shi, W. Zhou, A.-Y. Lu, W. Fang, Y.-H. Lee, A. L. Hsu, S. M. Kim, K. K. Kim, H. Y. Yang, L.-J. Li, J.-C. Idrobo, J. Kong, *Nano Lett.* **2012**, *12*, 2784–2791; d) A. M. Munshi, D. L. Dheeraj, V. T. Fauske, D.-C. Kim, A. T. J. van Helvoort, B.-O. Fimland, H. Weman, *Nano Lett.* **2012**, *12*, 4570–4576; e) P. K. Mohseni, A. Behnam, J. D. Wood, C. D. English, J. W. Lyding, E. Pop, X. Li, *Nano Lett.* **2013**, *13*, 1153–1161.

[12] Z. Liu, L. Song, S. Zhao, J. Huang, L. Ma, J. Zhang, J. Lou, P. M. Ajayan, *Nano Lett.* **2011**, *11*, 2032–2037.

[13] J. Hwang, M. Kim, D. Campbell, H. A. Alsalman, J. Y. Kwak, S. Shivaraman, A. R. Woll, A. K. Singh, R. G. Hennig, S. Gorantla, M. H. Rümmeli, M. G. Spencer, *ACS Nano* **2012**, *7*, 385–395.

[14] X. Li, W. Cai, J. An, S. Kim, J. Nah, D. Yang, R. Piner, A. Velamakanni, I. Jung, E. Tutuc, S. K. Banerjee, L. Colombo, R. S. Ruoff, *Science* **2009**, *324*, 1312–1314.

[15] P. R. H. Blasius, *Z. Math. Phys.* **1908**, *56*, 1–37.

[16] a) K. Tomioka, J. Motohisa, S. Hara, T. Fukui, *Jpn. J. Appl. Phys.* **2007**, *46*, L1102–L1104; b) S. A. Dayeh, D. Susac, K. L. Kavanagh, E. T. Yu, D. Wang, *Adv. Funct. Mater.* **2009**, *19*, 2102–2108.

[17] T. Akiyama, K. Sano, K. Nakamura, T. Ito, *Jpn. J. Appl. Phys.* **2006**, *45*, L275–L278.

[18] a) J. Johansson, K. A. Dick, P. Caroff, M. E. Messing, J. Bolinsson, K. Deppert, L. Samuelson, *J. Phys. Chem. C* **2010**, *114*, 3837–3842; b) R. E. Algra, M. A. Verheijen, M. T. Borgstrom, L.-F. Feiner, G. Immink, W. J. P. van Enckevort, E. Vlieg, E. P. A. M. Bakkers, *Nature* **2008**, *456*, 369–372.

[19] M. I. B. Utama, M. de la Mata, C. Magen, J. Arbiol, Q. Xiong, *Adv. Funct. Mater.* **2013**, *23*, 1636–1646.

[20] K. T. Chan, J. B. Neaton, M. L. Cohen, *Phys. Rev. B* **2008**, *77*, 235430.

[21] K. Reuter, M. Scheffler, *Phys. Rev. B* **2001**, *65*, 035406.

[22] S. Y. Tong, G. Xu, W. Y. Hu, M. W. Puga, *J. Vac. Sci. Technol. B* **1985**, *3*, 1076–1078.

[23] a) A. Ohtake, M. Ozeki, J. Nakamura, *Phys. Rev. Lett.* **2000**, *84*, 4665–4668; b) A. Taguchi, K. Kanisawa, *Appl. Surf. Sci.* **2006**, *252*, 5263–5266.

[24] a) M. C. Schabel, J. L. Martins, *Phys. Rev. B* **1992**, *46*, 7185–7188; b) L. X. Benedict, N. G. Chopra, M. L. Cohen, A. Zettl, S. G. Louie, V. H. Crespi, *Chem. Phys. Lett.* **1998**, *286*, 490–496; c) H. Rydberg, M. Dion, N. Jacobson, E. Schröder, P. Hyldgaard, S. I. Simak, D. C. Langreth, B. I. Lundqvist, *Phys. Rev. Lett.* **2003**, *91*, 126402.

[25] M. I. B. Utama, F. J. Belarre, C. Magen, B. Peng, J. Arbiol, Q. Xiong, *Nano Lett.* **2012**, *12*, 2146–2152.

[26] S. Cho, S. J. Youn, Y. Kim, A. DiVenere, G. K. L. Wong, A. J. Freeman, J. B. Ketterson, *Phys. Rev. Lett.* **2001**, *87*, 126403.

[27] S. Strite, M. S. Unlu, K. Adomi, G. B. Gao, A. Agarwal, A. Rockett, H. Morkoc, D. Li, Y. Nakamura, N. Otsuka, *J. Vac. Sci. Technol. B* **1990**, *8*, 1131–1140.

[28] Y.-H. Kim, M. J. Heben, S. B. Zhang, *Phys. Rev. Lett.* **2004**, *92*, 176102.

[29] D. H. Lee, J. Yi, J. M. Lee, S. J. Lee, Y.-J. Doh, H. Y. Jeong, Z. Lee, U. Paik, J. A. Rogers, W. I. Park, *ACS Nano* **2013**, *7*, 301–307.

© 2013 WILEY-VCH Verlag GmbH & Co. KGaA, Weinheim